Solar minimum exospheric neutral density near the subsolar magnetopause estimated from the XMM soft X-ray observations on 12 Nov 2008

J. Jung[1], H. K. Connor[1], J. A. Carter[2], D. Koutroumpa[3], C. Pagani[2], K. D. Kuntz[4] and more

[1]Geophysical Institute, University of Alaska Fairbanks, Fairbanks, AK, USA
[2]University of Leicester, Leicester, United Kingdom
[3]LATMOS-IPSL, CNRS, UVSQ Paris-Saclay, Sorbonne Universit, Guyancourt, France
[4]The Henry A. Rowland Department of Physics and Astronomy, Johns Hopkins University, Baltimore, MD, USA

Key Points:

- From 11 years of XMM-Newton X-ray observations, we identified 193 intervals that can be used to estimate the exospheric neutral density.
- We derived a solar minimum exospheric neutral density from the 12-Nov-2008 event using a global MHD model and a simplified exosphere model.
- The density estimate is 36.8 cm^{-3} near the subsolar magnetopause and is likely a lower limit value.

Corresponding author: J.Jung, jjung11@alaska.edu

Abstract

The Earth's magnetosheath and cusps emit soft X-rays due to the interaction between highly charged solar wind ions and exospheric hydrogen atoms. The LEXI and SMILE missions are scheduled to image the Earth's dayside magnetosphere system in soft X-rays and thus to investigate global-scale magnetopause reconnection modes under varying solar wind conditions. The exospheric neutral hydrogen density distribution is an important consideration in the calculation of X-ray emissivities. The value of this density at the subsolar magnetopause is of particular interest for understanding X-ray emissions near this boundary, and is used as a comparison between competing models of hydrogen distribution. This paper estimates the exospheric density during solar minimum by using X-ray Multimirror Mission (XMM) astrophysics observations. We searched 11 years of XMM soft X-ray data and provided a list of 193 events with a possible detection of X-rays of magnetospheric origin. These events occurred during relatively constant solar wind and interplanetary magnetic field conditions. During these events the location of the magnetopause was measured in-situ by heliospheric missions. Thus the location of the solar wind ions responsible for the magnetospheric emission are well constrained by observation. We detected one particular event on 12-Nov-2008 and and estimated an exospheric density using the Open Geospace Global Circulation Model (OpenGGCM) and a spherically symmetric exosphere model. The OpenGGCM magnetosheath parameters were used to disentangle soft X-rays of exospheric origin from the XMM signal. The lower limit of the exospheric density of this solar minimum event is 36.8 cm^{-3} at 10 R_E subsolar location.

1 Introduction

Understanding when, where, and how the magnetopause reconnection occurs is one of the most important topics in space physics. Tracking magnetopause reconnection on a global scale has been particularly challenging due to the lack of possibly simultaneous observations covering wide spatial regions of the magnetopause. Recently, soft X-ray imaging of the Earth's dayside system has been suggested as an innovative way to visualize the dayside magnetopause motion and thus infer the dayside reconnection mode (Connor et al., 2021).

A small portion of the solar wind plasma consists of highly charged ions, like O^{7+} or O^{8+}. The Earth's exosphere is the outermost layer of the atmosphere composed of mostly hydrogen atoms. When the ion collides with an exospheric neutral, the ion can capture an electron from the neutral atom. In the relaxation stage, soft X-rays are emitted:

$$S^{q+} + B \quad \rightarrow S^{(q-1)^{+*}} + B^{+} \tag{1}$$

$$S^{(q-1)^{+*}} \quad \rightarrow S^{(q-1)^{+}} + h\nu \tag{2}$$

where S is a solar wind origin ion, q is its charge state, * represents an excited state, and B is an exospheric neutral. This process is called Solar Wind Charge Exchange (SWCX) (Sibeck et al., 2018 and references therein).

After the first discovery of cometary X-ray emission (Lisse et al., 1996), Cravens (1997) suggested the SWCX process as a possible mechanism of such X-rays. Soon, Cravens et al. (2001) reported that the the diffuse background variation observed by the low-Earth orbit ROSAT (Rntgensatellit) astrophysics mission tracked variation in solar wind flux quite well, implying the Earth's atmosphere is a strong soft X-ray emitter. Subsequently, other astrophysics missions like XMM-Newton (Jansen et al., 2001; hereafter XMM), Suzaku (Mitsuda et al., 2007), and Chandra (Weisskopf et al., 2000) reported the detection of near-Earth soft X-ray emissions (K. Kuntz & Snowden, 2008,Carter et al., 2010,Ishikawa et al., 2013), which strongly motivates the space science community to study the solar wind - magnetosphere interaction through these signals. For this purpose, space missions

such as Cusp Plasma Imaging Detector (CuPID; `http://sites.bu.edu/cupid`) Cubesat observatory, Lunar Environment heliospheric X-ray Imager (LEXI; `http:sites.bu.edu/lexi`), and Solar wind - Magnetosphere - Ionosphere Link Explorer (SMILE; Branduardi-Raymont et al., 2018) have been planned and will be launched in the next few year.

The Earth's magnetosheath and cusps emit strongly in soft X-rays because both the exospheric hydrogen and the high-charge-state ions (i.e. the X-ray source particles) are more densely populated than in the upstream solar wind and the Earth's magnetosphere (Connor et al., 2021;Sibeck et al., 2018). The SWCX emission rate is controlled by three factors: neutral density, plasma ion density, and relative velocity between neutrals and ions (Connor & Carter, 2019;hereafter CC2019). While plasma density, velocity, and temperature in the magnetosphere are well understood by the heliophysics missions like Cluster, THEMIS, and MMS (Dimmock & Nykyri, 2013), neutral density in the magnetosheath is poorly understood due to severe lack of the exospheric observations above an altitude of 7 Earth radii(R_E). Under $7R_E$, Geocoronal Lyman-α observations have been a widely used data set for the neutral density studies (Bailey & Gruntman, 2011; Østgaard et al., 2003; Zoennchen et al., 2011, 2013, 2015, 2017; Baliukin et al., 2019). However, above 7 R_E interplanetary Lyman-α background overwhelms the geocoronal emission. Additionally, the dayside geocorona data are often contaminated by direct sunlight due to the close proximity of instrument's line-of-sight to the Sun. Recently, CC2019 suggested the SWCX observed by the XMM-Newton satellite as an alternative dataset to study the exospheric neutral density in the dayside magnetosheath.

In this paper, we surveyed ∼11 years of XMM observations, and created a new list of 193 potential near-Earth SWCX events that is ideal for our exospheric neutral density studies. Then, we selected one event that occurred during solar minimum and estimated a neutral density at 10 R_E subsolar location, considering that a typical subsolar magnetopause is located at about 10 R_E (Kivelson & Bagenal, 2014). Finally, we compare our solar minimum exospheric density to the solar maximum density of CC2019 as well as the neutral density in other literature.

This paper is structured as follows. Section 2 introduces data and models used in this study. Section 3 explains our methodology to derive an exospheric density from the XMM observations. Section 4 discusses our event selection process using the 11 years of XMM soft X-ray data. In section 5, we conduct a case study of the 12-Nov-2008 event and estimate a neutral density during the solar minimum. Section 6 compares our neutral density result with the ones in previous literature. Finally, section 7 summarizes our study.

2 Data and Model

2.1 XMM-Newton data

The XMM-Newton observatory (Jansen et al., 2001) is an observatory-class mission launched by the European Space Agency (ESA) in 1999 to investigate the astrophysical X-ray sky. Onboard XMM there are three imaging cameras that use X-ray CCD detectors at the focal plane, which make up the suite of instruments known as the European Photon Imaging Camera (EPIC). Two of the cameras are front-illuminated Metal Oxide Semiconductor (MOS) CCD arrays (Turner et al., 2001) and the other one uses back-illuminated pn CCD arrays called pn camera (Strüder et al., 2001). As XMM was designed to investigate distant X-ray astrophysical sources, many of which are extragalatic, the telescope field of view is narrow; 33' x 33' for MOS and 27.5' x 27.5' for pn. XMM has restricted view geometry due to the constraints imposed on the orientation of its solar panels. Depending on the geometry of the orbit and pointing requirement at the time of a particular observation, the telescope's line of sight may pass through the Earth's day-

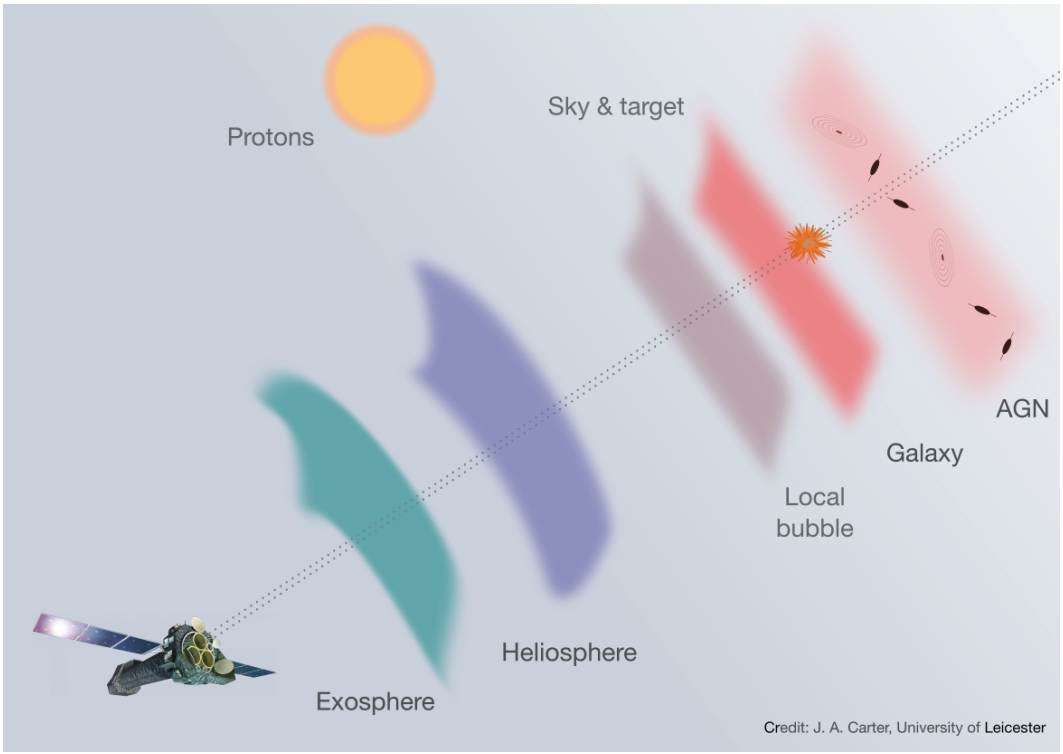

Figure 1. Various X-ray signals and the soft protons that create false counts in XMM X-ray cameras.

side magnetosheath, resulting in a foreground SWCX signal being imposed on that from the background X-ray sky, as sketched out in Figure 1.

Figure 1 summarizes various X-ray signals and the soft protons that create false counts in XMM X-ray cameras. The raw XMM measured signal includes different components, namely astrophysical point sources, instrumental background, sky background, heliospheric background, and near-Earth SWCX, and at times soft proton contamination. We need to identify the SWCX component for estimating the Earth's exospheric density. Section 5.1 explains details of the background removal process.

We downloaded Original Data Files (ODF) from the XMM Science Archive (XSA), and processed the data using the XMM Science Analysis System (SAS) software package version 18.0.0 (de la Calle, 2021), provided at the XMM data analysis web page: https://www.cosmos.esa.int/web newton/sas. We used the MOS full-frame observation data since some SAS commands needed in this study can be applied only to the full-frame mode data. This paper used the XMM observations between revolutions 21 and 1990, which corresponds to the period from the January 2000 to the October 2010.

2.2 OpenGGCM model

XMM can detect soft X-ray created in the magnetosheath as a result of the interaction between solar wind origin ions and exospheric neutrals. To derive an exospheric density, the plasma contributions should be disentangled from the XMM SWCX observations. We use OpenGGCM global magnetosphere - ionosphere MagnetoHydroDynamics (MHD) model to reproduce magnetosheath plasma condition during the XMM observation period. OpenGGCM calculates plasma density, velocity, temperature, and elec-

tromagnetic fields near the Earth's magnetosphere using the Solar Wind (SW) and IMF as input. This paper uses a stand-alone OpenGGCM model with the NASA OMNI SW/IMF data (King & Papitashvili, 2005). More details and applications of the OpenGGCM model can be found in Raeder et al. (2001, 2008) ; Cramer et al. (2017); Connor et al. (2012, 2014, 2015, 2016, 2021); Ferdousi and Raeder (2016); Jensen et al. (2017); Oliveira and Raeder (2015); Kavosi et al. (2018); Shi et al. (2017).

3 Methodology

This paper improves the method of CC2019 by considering soft X-ray signals in the 0.4 - 1.0 keV energy band. CC2019 considers only a few oxygen lines in the 0.5 - 0.7 keV band. Thus, their soft X-ray signals and subsequently their neutral density estimates tend to be sensitive to the oxygen abundance in the solar wind as reported in K. D. Kuntz et al. (2015). On the other hand, the 0.4 - 1.0 keV energy band includes various SWCX lines (Sibeck et al., 2018). The soft X-ray signals in this wide band are dependent on the total sum of high-charge state ions in the solar wind. Thus, our neutral density estimate is less sensitive to an individual ion abundance.

First, we assumed neutral density is spherically symmetric and inversely proportional to the distance cubed as in Cravens et al. (2001).

$$N_N = N_0 \left(\frac{10 R_E}{R} \right)^3 \quad [\mathrm{cm}^{-3}] \tag{3}$$

where N_0 is a neutral hydrogen density at 10 R_E subsolar point, i.e., at a typical subsolar magnetopause location (hereafter referred to as a characteristic neutral density), and R is a radial distance from the Earth's center in R_E.

Second, we calculate a soft X-ray emission rate for each SWCX spectral line j (R_j). We used following equation (K. Kuntz, 2019):

$$R_j = E_j \int N_N N_{sq} v_{eff} \sigma_{sq} Y_j \frac{ds}{4\pi} \quad [\mathrm{eV\ cm^{-2}\ s^{-1}\ sr^{-1}}] \tag{4}$$

where E_j is the emission line energy of transition j in eV, N_N is the exospheric neutral density in cm^{-3}, N_{sq} is the number density of a solar wind ion of species s in cm^{-3} and its charge state q(S^{q+}), v_{eff} is the relative velocity of the ion and the neutral (also called the effective velocity) in km/s, σ_{sq} is the cross section for the interaction between S^{q+} and hydrogen in cm^2, Y_j is the photon yield for the transition of $S^{(q-1)+}$ in number of photons, and ds is a spatial step for the integration along the line of sight.

Third, we define potential reaction rate (Q), the part we can calculate from the OpenGGCM MHD model:

$$Q = \int \frac{N_N}{N_0} N_p v_{eff} ds = \int \left(\frac{10 R_E}{R} \right)^3 N_p v_{eff} ds \quad [\mathrm{cm^{-1} s^{-1}}] \tag{5}$$

$$v_{eff} = \sqrt{v_p^2 + 3kT/m} \quad [km/s] \tag{6}$$

where m, N_p, v_p, and T are proton mass, density, drift velocity, and temperature, respectively, and k is the Boltzmann constant. The effective velocity (v_{eff}) depends on the plasma parameters and neutral velocity, but compared to the magnetosheath plasma velocity neutral velocity dependence is negligible.

Then, equation (4) becomes

$$R_j = \frac{1}{4\pi} Q N_0 E_j \frac{N_{sq}}{N_p} \sigma_{sq} Y_j \tag{7}$$

Here, we assumed that the ratio of high charge state ion to proton (N_{sq}/N_p) stays constant along the line-of-sight.

Fourth, we convert the emission rate R_j to a simulated soft X-ray count rate (C_{MHD}) based on the XMM instrument properties:

$$C_{MHD} = \sum_{E_j \in E} \frac{\Omega A_j}{E_j} R_j = \frac{1}{4\pi} \beta \Omega Q N_0 \quad [cts/s] \tag{8}$$

where Ω is the XMM field-of-view in sr and A_j is the effective area of XMM in cm^2 at the X-ray energy E_j. The summation is done over all the spectral lines of energy E_j inside the energy band of our interest (0.4 - 1.0 keV). The effective scale factor (β) considers charge exchange mechanism of all the individual SWCX lines in our energy band:

$$\beta = \sum_{E_j \in E} A_j \frac{N_{sq}}{N_p} \sigma_{sq} Y_j \ [\mathrm{cm}^4] \tag{9}$$

CC2019 used an effective scale factor α that considers only a weight-averaged emission line at 590.5 eV because they focus on the X-ray emission in a narrow energy band (0.5-0.7 keV). Since O^{7+} and O^{8+} are the main contributor to this energy band, the X-ray count rates become very sensitive to the oxygen abundance in solar wind (K. D. Kuntz et al., 2015), which may break the assumption of a constant oxygen-to-hydrogen ratio used in CC2019. To avoid such problem, we focus on a wider energy band (0.4 - 1 keV) that includes emission lines from various charge-state solar wind ions (e.g., C^{6+}, N^{6+}, N^{7+}, Ne^{9+}, S^{10+}, O^{7+},and O^{8+}). The total abundance of all the SWCX source ions in solar wind is expected to be more stationary than the abundance of oxygen itself in the solar wind, thus better satisfying our assumption and subsequently providing more accurate neutral density estimate. Thus, the effective scale factor β is better suited for our wide-band X-ray study than α .

Effective area A_j can be obtained from the XMM Auxiliary Response File (ARF). ARF file contains table including the effective area information at each energy. We assumed that these two parameters have a negligible error. For the ratio of highly charged ion to proton (N_{sq}/N_p), the CX cross section (σ_{sq}), and the photon yield (Y_j), we used data of Koutroumpa et al. (2006) (assuming slow solar wind). The resultant β is 1.53×10^{-16} cm^4.

Finally, assuming that equation (3) is good representation of our exospheric density distribution, the modeled count rate (C_{MHD}) should be equal to the SWCX count rates observed by XMM (C_{SWCX}), $C_{MHD} = C_{SWCX}$. Using equation (8), the characteristic density N_0 becomes

$$N_0 = \frac{4\pi}{\beta \Omega Q} C_{SWCX} \tag{10}$$

4 Event Selection

Carter et al. (2011) selected 103 XMM soft X-ray observations that showed temporal variability in the 0.5-0.7 keV energy band compared to the 2.5-5.0 keV continuum band. These observations are considered as the near-Earth SWCX events because the astronomical soft X-rays are almost constant within a time scale of several hours to a few days. CC2019 selected two of these observations and derived solar maximum neutral densities. However, the event selection criteria in Carter et al. (2011) tends to find cases during dynamic SW/IMF conditions that may complicate the reproduction of magnetosheath conditions, and thus the calculation of plasma contribution to the near-Earth soft X-ray emissions. To avoid such problem, we searched 11 years of XMM observations and create a new list of XMM events suited for our exospheric density studies. The following four steps are taken for the new event selection.

First, we selected the potential near-Earth SWCX events by searching for the times when XMM looks through the dayside magnetosheath, where strong soft X-ray emissions are expected, during relatively constant solar wind and IMF conditions. We avoided the dynamic upstream conditions because a global MHD model may have difficulty reproducing complex solar wind - magnetosphere interaction. Figure 2a shows the examples of selected (left) and not selected (right) XMM events under our selection process. Orange lines represent the bow shock locations at the start (solid) and at the end (dashed) of the XMM observation time, calculated from Jeřáb et al. (2005) using the NASA OMNI SW/IMF data (King & Papitashvili, 2005). Similarly, red lines are the magnetopause locations at the start (solid) and at the end (dashed) of the XMM observation time, calculated from Shue et al. (1998) model. The blue and black lines are the XMM orbit and look direction during the observation period, respectively. We select the event in the left panel of Figure 2A because the dayside boundaries are relatively stationary during the observation period and because XMM looks through the dayside magnetosheath.

Second, we removed events where bright, and particularly extended X-ray sources, are found in the Field-of-View (FOV). Figure 2B shows XMM examples selected (left) and not selected (right) from this process. The near-Earth SWCX signals are derived from the background signals, for example, the blue region in the left panel of Figure 2B. If the X-ray sources are very bright and/or extended, for example in the right hand panel of fig2B, photons from astrophysical source may be accidentally incorporated into the backgrounnd signal, even after filtering for astrophysical sources is applied. To obtain more accurate SWCX signals, we exclude the XMM observations of bright sources from further analysis.

Third, we excluded the XMM events that are badly contaminated by soft proton flaring. Energetic protons of a few hundred keV, called soft protons, can reach the XMM camera detectors and falsely create a signal at the detector plane. At times, the soft proton signals are very strong and dominate other X-ray sources. This is known as soft proton flaring (Lumb et al., 2002 ; Walsh et al., 2014) and has to be removed from our event selection. Using HEASARC XMM trend data, we compared two light curves (one corresponding to the in field-of-view, the other the out of field-of-view) for a band between 2.5 - 12 keV, and count rate histogram for the in field-of-view light curve. If the observation is not affected by soft proton flaring, the count rate histogram should have a Gaussian profile. We excluded observations heavily affected by soft proton flaring. Out of FOV light curves are used later to identify particle background contamination. This second and third steps have been done by visual inspection.

Finally, we selected the XMM observations when a solar wind monitor like ACE and WIND provides good quality solar wind/IMF data and when a heliophysics satellite like Cluster, Geotail, and THEMIS provides in-situ magnetosheath plasma observations. The solar wind and IMF data are used as input for the OpenGGCM model, and the in-situ magnetosheath plasma data are used to validate the model results.

From the XMM observations between 2000 and 2010, we have found 193 potential SWCX events that are well suited for our density derivation techniques. Table S1 shows the list of all the events for future exosphere density studies. This paper selects an event on 12 Nov 2008 for estimating a solar minimum exospheric density (XMM observation number 0551860501).

5 Case study of the 12-Nov-2008 event

5.1 Extraction of the near-Earth SWCX counts

As discussed in Section 2.1, the raw XMM data includes soft proton contamination, astrophysical point sources, instrumental background, sky background, heliospheric background, and near-Earth SWCX signals. In this section, we follow general procedures

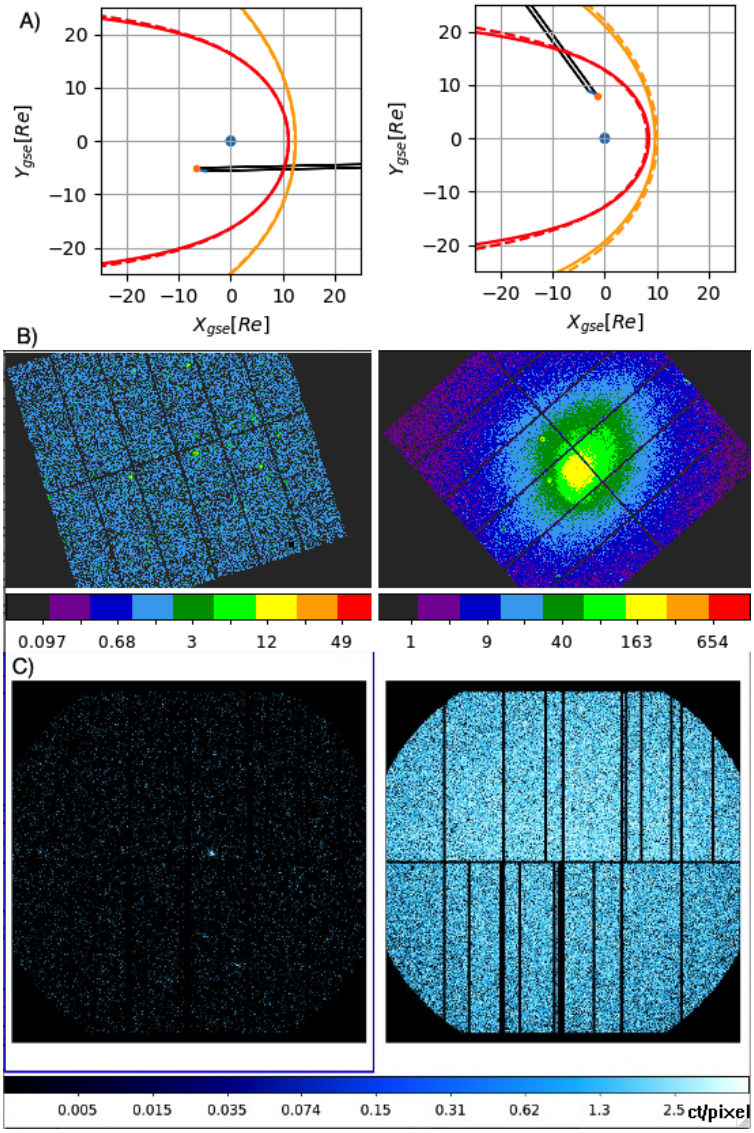

Figure 2. Example of XMM observation selection process. A) Look direction inspection. B) Visual image inspection. C) Soft proton flaring check. Unit of X-ray images is counts /pixel. For each panel, observation on the left side is what we chose and one on the right side is what we excluded. Detailed method is described in the text.

used in the astrophysics community to estimate the contribution of background and noise components and thus derive the terrestrial signals from the raw XMM observation on 12 Nov 2008.

First, we extracted a total XMM background rate by removing a soft proton contamination period and the signal from astrophysical point sources in XMM data. Although we removed periods of soft proton flaring, there can be variation on longer timescales that is missed by our method; some residual soft proton flaring may remain in our data, but will not have a time variation on the scales of interest. To remove this additional contamination period, we calibrated event files from original data files using SAS tasks *emproc*. Then, we created good-time-interval (GTI) file using *tabgtigen*, and applied it to the event file to remove contaminated time intervals. After obtaining the counts from the GTI, we removed astrophysical point sources in the field of view using *edetect_chain* to detect point sources in the image and *evselect* to generate a region file and subtracted them from the original event file. We applied a 35 arcsec extraction radius about each point source. After the automatic astrophysical point source removal process, we visually checked an image generated from the XMM cleaned data, after which we applied a large circle of 500 arcsec radius, to remove an astrophysical source found near the boresight of the telescope that had not been completely removed during the previous steps. From this first step, we estimated a total XMM background count of the 12-Nov-2008 event at 4369 counts for 3.3 hours of exposure time.

Second, we estimated instrumental background caused by high-energy particles that produce charge directly in the CCDs, and particle-induced X-rays generated inside the camera. EPIC instrumental background files can be obtained with the filter wheel in a closed position (K. Kuntz & Snowden, 2008). A Filter Wheel Closed (FWC) data repository is available through XMM Science Operation Centre from EPIC background Analysis web pages. Since SAS v.16, the task *evqpb* is available to generate a tailored FWC event file corresponding to an observation. It is typical in X-ray analysis that the FWC derived background spectrum needs rescaling to get a more representative background for the observation under study. We scaled the background spectrum to the science spectrum for each observation in the high energy band of 7.5-9.2 keV, where the contribution is believed to be entirely from the instrumental background. The total instrumental background rate for the 12-Nov-2008 event after this step is 2037 counts.

Third, we estimated the sky background. We utilized a HEASARC X-ray background command line tool (`https://heasarc.gsfc.nasa.gov/Tools/xraybg\_help.html\#command`) to get the ROSAT all sky survey (RASS) data (Snowden et al., 1997) for the given galactic coordinate. Following Galeazzi et al. (2007), we modelled the ROSAT diffuse spectrum with three components. Two of them are unabsorbed and absorbed plasma components, representing X-ray emissions from the diffuse local interstellar and more distant galactic halo components, respectively. We used the APEC (Smith et al., 2001) model within *XSPEC*(`https://heasarc.gsfc.nasa.gov/xanadu/xspec/`) to calculate these plasma components. The last component is absorbed power law, representing the unresolved extragalactic X-ray background. We calculated the last component using *wabs* model (Morrison & McCammon, 1983) by considering absorption by neutral hydrogen in the Galaxy along the line-of-sight of our XMM event. Constant sky background is expected throughout our event because the satellite pointing is fixed and because our event is only $\sim$3.3 hours long, much shorter than time scale of sky background variation. As we will note later, the sky background obtained from the ROSAT data may contain some fraction that originates from the heliosphere. The total sky background for the 12-Nov-2008 event is 1459 counts.

Fourth, we subtracted a heliospheric background component. SWCX is also produced within the heliosphere via a charge exchange interaction between interplanetary neutrals and solar wind plasma. This signal depends on neutral and plasma density distribution along the instrument's line-of-sight at the time of observation (Koutroumpa

Table 1. Summary of the soft X-ray background counts for the 12 Nov 2008 event.

Component	Counts	Contribution(%)
Total(C_{bgd})	4369	100
Instrumental (C_{inst})	2037	46.6
Astronomical (C_{sky})	1459	33.4
Heliospheric (C_{helio})	771	17.7
SWCX (C_{SWCX})	102	2.3

et al., 2006). The heliospheric hydrogen and helium distributions were calculated as in Koutroumpa et al. (2006), based on 'hot model' simulations from Lallement et al. (1985) and Dalaudier et al. (1984), respectively. The distributions were adjusted to solar activity corresponding to late 2008. By assuming a solar wind flux of 2.0×10^8 cm^{-2} s^{-1}, we obtained a total heliospheric signal of the 12-Nov-2008 event at 771 counts.

Finally, we obtained the near-Earth SWCX of our event by subtracting instrumental, sky, and heliospheric backgrounds from the total XMM background counts. The resultant terrestrial SWCX counts is 102 counts for the 3.3-hour observation period on 12 Nov 2008. Table 1 summarizes all the background components.

5.2 Neutral density estimation

We derived an exospheric neutral density from the 12 Nov 2008 event. About 3.3 hours of soft X-ray data (03:43 - 07:03 UT) were available from EPIC MOS observations. Figure 3 summarizes the orbital and observational details of the spacecraft observations, and the IMF and solar wind conditions during the period of interest. Figure 3A displays the XMM orbit (blue line), its look direction (black line), the THEMIS-B orbit (green line), magnetopause location (red line), and the bow shock location (yellow line) projected on the GSE XY (left) and XZ (right) planes during the observation period. The orange/red dots present the starting locations of XMM/THEMIS B for this event, respectively. Figure 3B shows, from top to bottom, IMF, solar wind velocity, number density, plasma pressure ($P = nkT$), and solar wind proton flux ($n_{sw}V_{sw,x}$). Green and gray shaded areas indicate intervals of XMM near-Earth SWCX observation and the THEMIS-B magnetosheath observation, respectively.

XMM was located near the southern magnetosphere, and looks through the dusk-side, northern magnetosheath. XMM moves slightly southward and away from the sun. During the XMM observation, THEMIS-B crosses the dawnside magnetosheath, providing not only the plasma conditions in the magnetosheath but also the locations of magnetopause and bow shock. We use these THEMIS-B data for model validation and the model-induced error analysis in our density estimates. Throughout this short observation, solar wind condition and IMF magnitude are relatively constant. We simulated the 12 Nov 2008 event by using the solar wind and IMF conditions in Figure 3B as input for OpenGGCM.

Figure 4 compares the OpenGGCM data (green) with the THEMIS B observations (blue). Plasma density (N_p), effective velocity (V_{eff}), effective flux ($N_p\times v_{eff}$), and model-to-data ratio of the effective flux are shown from top to bottom. We select these parameters for comparison because plasma density and effective velocity are key parameters of potential reaction rate Q and thus contributes to the estimation of characteristic neutral density N_0, as seen in equations (5) and (10). While THEMIS B crosses the magnetosheath (gray shaded area), the model-to-data ratio is nearly one, suggesting that the MHD model reasonably reproduces the magnetosheath plasma conditions.

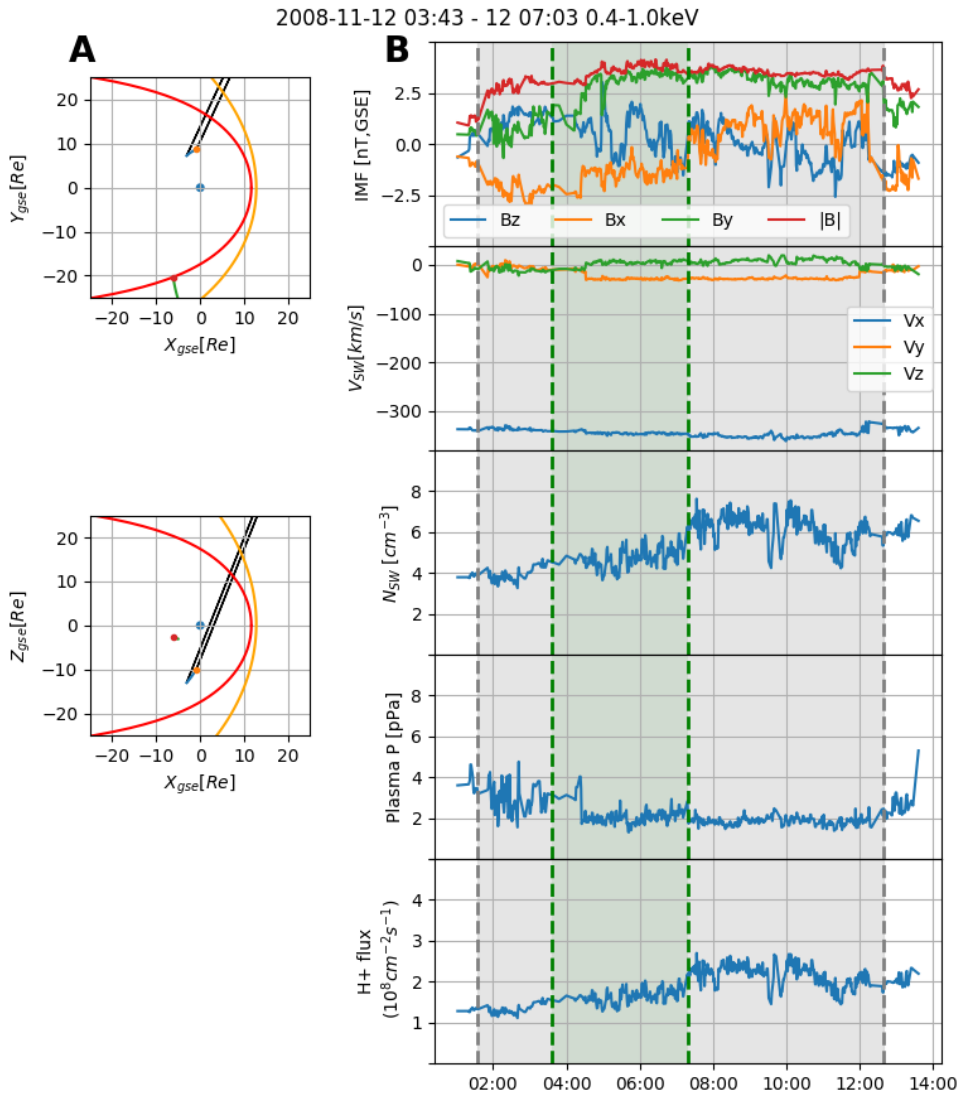

Figure 3. A) XMM orbit (blue), its look direction (black), and THEMIS B orbit (green) projected on the GSE XY (top) and XZ (bottom) planes. The starting location of XMM and THEMIS B are shown as orange and red dots, respectively. Yellow and red curves show bow shock derived from Jeřáb et al. (2005) and magnetopause derived from Shue et al. (1998). B) Solar wind and IMF conditions during XMM observation (green area) and during THEMIS B magnetosheath crossing (grey area). IMF, solar wind velocity, number density, plasma pressure, and solar wind proton flux in GSE coordinates are shown from top to bottom.

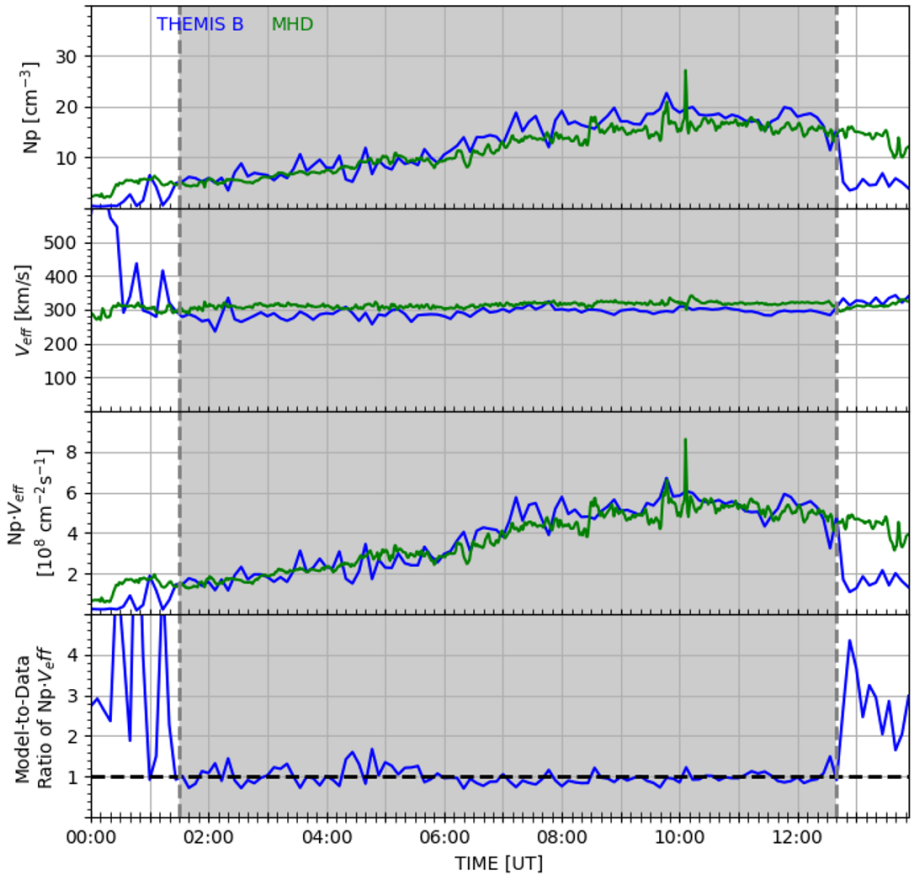

Figure 4. Comparison of OpenGGCM results (green) with THEMIS B plasma observation (blue) on 12 Nov 2008. From top to bottom, plasma density, effective plasma velocity, effective flux, and model-to-data ratio of the effective flux are shown. The gray shaded area indicates when the THEMIS B passes through the magnetosheath. The dashed black line in the bottom panel shows a line at which the model-to-data ratio equals one.

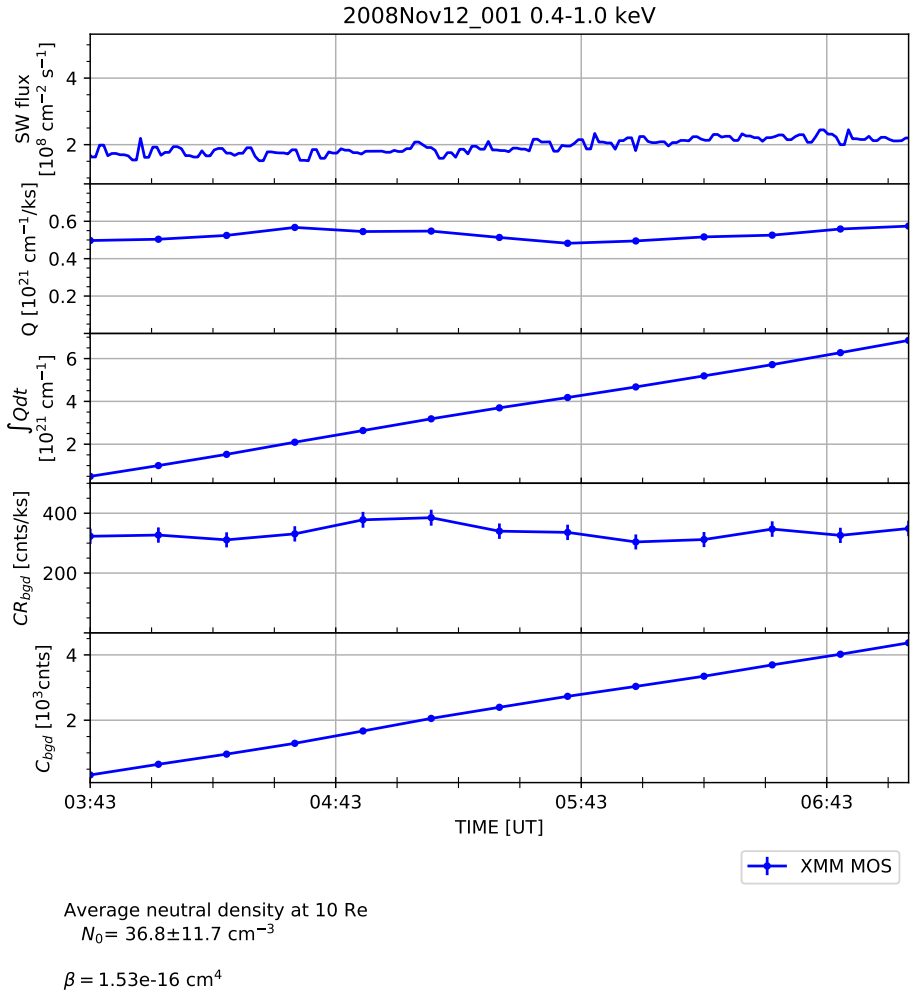

Figure 5. Modeled potential reaction rate and total XMM background counts of the 12 Nov 2008 event. From top to bottom, solar wind flux, modeled potential reaction rate (Q), accumulated potential reaction rate ($\int Qdt$), total XMM background count rate (C_{bgd}), and accumulated XMM count rates ($\int C_{bgd}$) are shown. The effective scale factor β is shown at the bottom of the figure.

Figure 5 presents solar wind flux, modeled potential reaction rate (Q), accumulated potential reaction rate ($\int Qdt$), XMM-background count rate (C_{bgd}), and accumulated XMM background counts ($\int C_{bgd}dt$) from top to bottom. C_{bgd} is the total XMM background counts after the astrophysical point source removal, including not only the near-Earth SWCX signal but also the astronomical, heliospheric, and particle background. Fluctuation in C_{bgd} can be considered due to the near-Earth SWCX variation because other background counts vary in a much longer time scale than the ∼3.3 hours of our observation period. Solar wind flux is nearly constant during this event, so are the modeled potential reaction rate and the XMM background counts.

The total near-Earth SWCX count of the 12-Nov-2008 event is 102, very weak compared to the count rates in CC2019 that go up to 250 counts/ks. To increase a source-to-noise ratio of the XMM data, we used total accumulated potential reaction rate ($\int Qdt$) and total near-Earth SWCX (C_{SWCX}) during the 3.3 hour event. From equation (10), we obtained an exospheric density near the subsolar magnetopause at 36.8 cm^{-3}.

5.3 Error analysis

We calculate the uncertainty of the neutral density measurement by estimating and propagating the error of near-Earth XMM counts (C_{SWCX}) obtained from the soft X-ray background removal process and the error of potential reaction rate (Q) from the model-data magnetosheath boundary mismatch.

As described in section 5.1, we obtained C_{SWCX} by subtracting instrumental background (C_{inst}), sky background (C_{sky}), and heliospheric background (C_{helio}) from the total XMM background counts (C_{bgd}).

$$C_{SWCX} = C_{bgd} - C_{inst} - C_{sky} - C_{helio} \tag{11}$$

The error in C_{SWCX} is calculated by propagating Poisson errors of each component:

$$E_{SWCX} = \sqrt{E_{bgd}^2 + E_{inst}^2 + E_{sky}^2 + E_{helio}^2} \tag{12}$$

The relative error (E_{SWCX}/C_{SWCX}) for the 12-Nov-2008 event is estimated at 18%.

Soft X-ray emission of this event mostly comes from the magnetosheath (see the XMM line-of-sight in Figure 3a), and therefore depends on the magnetosheath plasma flux and the magnetosheath thickness along the line-of-sight. The model-data comparison in Figure 4 shows that OpenGGCM reasonably reproduces the magnetosheath plasma flux. However, OpenGGCM shows a wider magnetosheath than the THEMIS observation. During this event, THEMIS B observes multiple magnetopause crossing from 00:30 UT until it fully enters the magnetosheath at 01:30 UT. At ∼12:40 UT, THEMIS crosses the bow shock and enters the upstream solar wind. However, the simulated spacecraft in OpenGGCM crosses the magnetopause around 00:20 UT, earlier than THEMIS B, and stays still in the magnetosheath at 12:40UT when THEMIS B went out to solar wind. This thicker magnetosheath in the MHD model over-estimates Q due to a longer integration path, and subsequently underestimates exosphere density (N_0) in equation (10). The error on the estimate of Q caused by the model-data boundary mismatch must be addressed. However, due to the limited number of satellites, it is difficult to know the 3-dimensional locations of magnetopause and bow shock for the entire observation period.

We calculated the maximum error in Q assuming that the difference between the modeled and observed boundaries stays constant throughout the observation period. We used the THEMIS magnetopause and bow shock crossings at 01:34 and 12:40 UT, respectively, as reference points, calculating the distances between modeled and observed boundaries. Then, we shifted the modeled magnetopause sunward and the modeled bow

shock earthward by the amount of the boundary differences, obtaining the narrowest possible magnetosheath during the observation period. Finally, we obtained Q from the narrowest magnetosheath and calculate the relative difference between Qs from the unmodified and modified magnetosheath as the maximum possible error in Q. The resultant maximum error in Q is 23%.

By propagating 23% of Q error and 18% of C_{SWCX} error, we obtained 29% of the neutral density error. The resultant neutral density and its error are estimated at 36.8 $\pm$ 11.7 cm^{-3}.

We would like to note that the characteristic exospheric density (N_0) estimated from the 12-Nov-2008 event is likely to be a lower limit value. Firstly, the sky background obtained from the ROSAT data (C_{sky}) may contain some fraction that originates from the heliosphere. This may lead to an over subtraction of C_{helio} and thus underestimation of C_{SWCX} and N_0. Secondly, β is likely lower than the one used in our study, thus underestimating N_0. Due to the severe lack of solar wind heavy ion data, previous literature has shown discrepancies in the high-charge state ion abundances in the solar wind (Whittaker & Sembay, 2016,Pepino et al., 2004,Cravens et al., 2001,Robertson et al., 2006,Carter et al., 2010,Koutroumpa et al., 2006), causing difficulties in calculating β. We used Koutroumpa et al. (2006) because it provides a comprehensive list of high-charge state ions, thus well suited for our wide-band soft X-ray analysis. However, we found that some ion abundances in Koutroumpa et al. (2006) are larger than the ones in other literature, thus leading to a large β. Finally, overestimation of potential reaction rate (Q) in the MHD model is supposed to create only a positive error. However, the error analysis used in our study naturally assumes that both positive and negative errors are possible in Q. The upper error bar should be more emphasized than the lower error bar when interpreting our density estimate. In conclusion, our neutral density estimates can be considered as a lower limit estimates at $10R_E$ subsolar location. The actual density is likely to be larger than 36.8 cm^{-3}.

6 Discussion

The exospheric density above $8R_E$ geocentric distance and its variation during a solar cycle are poorly understood due to severe lack of the outer exosphere data. The geocoronal Lyman-α emission has been most widely used dataset for the exosphere density studies, but its signal becomes weaker than the interplanetary Lyman-α background signals in the region above $8R_E$ geocentric distance, thus not ideal for studying the neutral density near the subsolar magnetopause (Connor et al., 2021). CC2019 and Fuselier et al. (2010, 2020) showed that from the XMM soft X-ray observations and the Interstellar Boundary EXplorer (IBEX) Energetic Neutral Atom (ENA) observations of the Earth's magnetosheath it is possible to derive the exospheric density at $10R_E$ subsolar location, i.e., a typical location of subsolar magnetopause. Their density estimates range from 4 to 58 cm^{-3} with the lowest end coming from the IBEX data (Fuselier et al., 2010) and the highest end from the XMM data (Connor & Carter, 2019). CC2019 considered solar cycle as a possible reason of this large discrepancy by pointing out that the IBEX cases in Fuselier et al. (2010) occurred during solar minimum, while the XMM cases in CC2019 occurred near solar maximum. However, Fuselier et al. (2020) derived 11-18 cm^{-3} of a solar maximum neutral density from an IBEX event on 04 Nov 2015, that is not much different from 4-11 cm^{-3} of solar minimum density obtained from 5 IBEX events in 2008 and 2009. They concluded that the dayside outer exosphere is weakly dependent on the solar cycle, although they cautiously pointed out that the F10.7 solar irradiance index of their solar maximum event is 110 solar flux unit (sfu), lower than 144.4 and 205.8 sfu of the two solar maximum events of CC2019.

The large density discrepancy between the XMM of this result and IBEX studies still exist, partly due to inherent difference of the two dataset and partly due to differ-

ent density derivation techniques. For example, the ENA observations are very sensitive to plasma velocity distributions (Connor et al., 2021). For accurate neutral density estimation, a realistic magnetosheath model and sophisticated analysis of magnetosheath ion flux that move toward the IBEX detector are necessary. However, the IBEX neutral density studies calculate the magnetosheath ion flux along a simplified IBEX look direction by assuming time-independent, homogeneous magnetosheath plasma conditions (Fuselier et al., 2010) or by using a time-independent, gas-dynamic magnetosheath model (Fuselier et al., 2020), thus omitting the comprehensive analysis to account for the Compton-Getting effect (i.e., the relative motion of the magnetosheath plasma and the IBEX ENA detector) On the other hand, the XMM mission is designed for optimizing the signal to noise for astrophysical sources with a pencil beam field-of-view and a long observation time of a specific target. As a result, we had to go through a long background removal processes as described in section 5.1. This observational difficulty will be addressed to some extent by the LEXI and SMILE missions that will observe the magnetosheath as a main target. Additionally, the abundance of the high charge state ions required for the charge exchange process needs to be studied in further detail, highlighting the need for an independent and new space mission with a heavy ion detector, for most accurate calculation of β and N_0. Our study focused on the lower limit of possible exospheric neutral density during solar minimum with the selection of a large β, in an attempt to reduce the large discrepancy between the XMM and the IBEX studies. We found that our density estimate, 36.8 $\pm$ 11.7 cm^{-3}, are still higher than 4-17 cm^{-3} of Fuselier et al. (2010, 2020) but comparable to other geocorona studies, 24-46 cm^{-3} of Zoennchen et al. (2015) and 41 cm^{-3} of Baliukin et al. (2019), although these geocoronal studies may have large uncertainties due to their observational difficulties above $8R_E$ geocentric distances.

Although the direct comparison of XMM and IBEX densities is troublesome, comparison between the XMM observations are still meaningful since it clears some ambiguity coming from the different datasets and different density derivation techniques. Considering error bars, our solar minimum neutral density is consistent with 39.9$\pm$8.0 and 57.6$\pm$8.0 cm^{-3} of solar maximum neutral densities from the two CC2019 events. This seems to support a similar conclusion of Fuselier et al. (2020), i.e., minimal response of outer exospheric density to solar cycle. However, only a handful of XMM events (2 for solar maximum and 1 for solar minimum) and IBEX events (1 for solar maximum and 5 for solar minimum) have been studied so far. More statistical approaches are needed before testing this hypothesis. Our list of potential XMM-SWCX events in the supplementary document would be a useful source for such a statistical analysis. For future work, we will conduct more case studies using our list and investigate the solar cycle - neutral density relation near the subsolar magnetopause.

7 Summary

The LEXI and SMILE missions will observe the Earth's magnetosheath and cusps through X-ray emissions after their respective launches in 2023 and 2024. Measurements of the near-Earth X-ray signal from these missions will allow the derivation of the neutral density near the subsolar magnetopause, an important parameter in the study of the atmosphere-solar wind interaction. We utilized the magnetosheath soft X-ray observations obtained from the XMM astrophysics mission to calculate a solar minimum exospheric neutral density at 10 R_E subsolar location, where the subsolar magnetopause is typically located. First, we surveyed $\sim$11 years of XMM observations, and found 193 potential near-Earth SWCX events that are well suited for our density derivation technique. The event list is provided in the supplementary document for future exosphere studies. Second, we estimated the exospheric density from a solar minimum event on 12 Nov 2008 by improving the density derivation technique of CC2019. We obtained near-Earth soft X-ray data from the raw XMM observations. Then, we subtracted the magnetosheath

plasma contribution from the X-ray signals using the OpenGGCM simulation and derived an exospheric density of 36.8 ± 11.7 cm^{-3} at 10 R_E subsolar location during solar minimum. Due to a potential overestimation of heliospheric signals (C_{helio}), effective scale factor (β), and potential reaction rate (Q), our density should be considered as a lower limit. The actual neutral density is likely to be larger than 36.8 cm^{-3}. Last, we discussed our results in comparison with the previous literature. Our neutral density is within the range of previously reported densities, 4-59 cm^{-3}. Our solar minimum value is consistent with the values at solar maximum of 39.9-57.6 cm^{-3} in CC2019, considering the error bars. This implies minimal impact of solar cycle on the outer exosphere density as suggested by Fuselier et al. (2020). However, only a handful of event studies have been previously reported in the literature. More statistical analysis is needed in future to conclude the solar cycle - neutral density relation. The neutral density behavior of the outer exosphere will help us understand the Earth's atmospheric loss due to dynamic space environment and thus to infer the whole evolutionary history of the Earth's atmosphere as well as other planetary atmospheres.

Acknowledgments

This work was supported by the NSF grant AGS-1928883 and the NASA grants, 80NSSC18K1043 and 80NSSC20K1670, and 80MSFC20C0019. Hyunju K. Connor gratefully acknowledges support from the NSF grant OIA-1920965 and the NASA grants, 80NSSC18K1042 and 80NSSC19K0844. We also acknowledge the support from the International Space Science Institute on the ISSI time 492, title "the Earth's Exosphere and its Response to Space Weather".

We appreciate Jochen Zoennchen at Argelander Institut fr Astronomie, and Igor Baliukin at Space Research Institute for useful discussions on the X-ray background signals. Dimitra Koutrompa's heliospheric SWCX modeling work was supported by CNES and performed with the High Performance Computer and Visualisation platform (HPCaVe) hosted by UPMC-Sorbonne Universités. JAC gratefully acknowledges support from the UK Science Technology Facilities Council (STFC) consolidated grant ST/N000429/1.

OMNI solar wind and IMF data are available at `https://omniweb.gsfc.nasa.gov` website, XMM-Newton data are available at `https://xmm.vilspa.esa.es/external/xmm_data_acc/xsa/index.shtml` website, and OpenGGCM results are available at . HEASARC tooklit can be found via `https://heasarc.gsfc.nasa.gov/ftools/`, XMM Science Analysis System can be found at `https://www.cosmos.esa.int/web/xmm-newton/sas`. XMM-Newton observations data can be downloaded from `http://nxsa.esac.esa.int/nxsa-web/#home`. XSPEC is available at `https://heasarc.gsfc.nasa.gov/xanadu/xspec/`

References

Bailey, J., & Gruntman, M. (2011). Experimental study of exospheric hydrogen atom distributions by lyman-alpha detectors on the twins mission. *Journal of Geophysical Research: Space Physics*, *116*(A9).

Baliukin, I. I., Bertaux, J.-L., Quémerais, E., Izmodenov, V., & Schmidt, W. (2019). Swan/soho lyman-α mapping: The hydrogen geocorona extends well beyond the moon. *Journal of Geophysical Research: Space Physics*, *124*(2), 861–885.

Branduardi-Raymont, G., Wang, C., Dai, L., Donovan, E., Li, L., & Sembay, S. (2018). Smile definition study report. *ESA/SCI (2018)*, *1*.

Carter, J., Sembay, S., & Read, A. (2010). A high charge state coronal mass ejection seen through solar wind charge exchange emission as detected by xmm–newton. *Monthly Notices of the Royal Astronomical Society*, *402*(2), 867–878.

Carter, J., Sembay, S., & Read, A. (2011). Identifying xmm-newton observations affected by solar wind charge exchange–part ii. *Astronomy & Astrophysics*, *527*,

A115.

Connor, H., & Carter, J. A. (2019). Exospheric neutral hydrogen density at the nominal 10 re subsolar point deduced from xmm-newton x-ray observations. *Journal of Geophysical Research: Space Physics*, *124*(3), 1612–1624.

Connor, H., Raeder, J., Sibeck, D., & Trattner, K. (2015). Relation between cusp ion structures and dayside reconnection for four imf clock angles: Openggcm-ltpt results. *Journal of Geophysical Research: Space Physics*, *120*(6), 4890–4906.

Connor, H., Raeder, J., & Trattner, K. (2012). Dynamic modeling of cusp ion structures. *Journal of Geophysical Research: Space Physics*, *117*(A4).

Connor, H., Sibeck, D., Collier, M., Baliukin, I., Branduardi-Raymont, G., Brandt, P., ... others (2021). Soft x-ray and ena imaging of the earth's dayside magnetosphere. *Journal of geophysical research. Space physics*, *126*(3).

Connor, H., Zesta, E., Fedrizzi, M., Shi, Y., Raeder, J., Codrescu, M. V., & Fuller-Rowell, T. J. (2016). Modeling the ionosphere-thermosphere response to a geomagnetic storm using physics-based magnetospheric energy input: Openggcm-ctim results. *Journal of Space Weather and Space Climate*, *6*, A25.

Connor, H., Zesta, E., Ober, D., & Raeder, J. (2014). The relation between transpolar potential and reconnection rates during sudden enhancement of solar wind dynamic pressure: Openggcm-ctim results. *Journal of Geophysical Research: Space Physics*, *119*(5), 3411–3429.

Cramer, W. D., Raeder, J., Toffoletto, F., Gilson, M., & Hu, B. (2017). Plasma sheet injections into the inner magnetosphere: Two-way coupled openggcm-rcm model results. *Journal of Geophysical Research: Space Physics*, *122*(5), 5077–5091.

Cravens, T. (1997). Comet hyakutake x-ray source: Charge transfer of solar wind heavy ions. *Geophysical Research Letters*, *24*(1), 105–108.

Cravens, T., Robertson, I., & Snowden, S. (2001). Temporal variations of geocoronal and heliospheric x-ray emission associated with the solar wind interaction with neutrals. *Journal of Geophysical Research: Space Physics*, *106*(A11), 24883–24892.

Dalaudier, F., Bertaux, J., Kurt, V., & Mironova, E. (1984). Characteristics of interstellar helium observed with prognoz 6 58.4-nm photometers. *Astronomy and Astrophysics*, *134*, 171–184.

de la Calle, I. (2021). Users guide of the xmm-newton science analysis system. *Issue 16.0, 2021 (ESA: XMM-Newton SOC)*.

Dimmock, A., & Nykyri, K. (2013). The statistical mapping of magnetosheath plasma properties based on themis measurements in the magnetosheath interplanetary medium reference frame. *Journal of Geophysical Research: Space Physics*, *118*(8), 4963–4976.

Ferdousi, B., & Raeder, J. (2016). Signal propagation time from the magnetotail to the ionosphere: Openggcm simulation. *Journal of Geophysical Research: Space Physics*, *121*(7), 6549–6561.

Fuselier, S., Dayeh, M., Galli, A., Funsten, H., Schwadron, N., Petrinec, S., ... others (2020). Neutral atom imaging of the solar wind-magnetosphere-exosphere interaction near the subsolar magnetopause. *Geophysical research letters*, *47*(19), e2020GL089362.

Fuselier, S., Funsten, H., Heirtzler, D., Janzen, P., Kucharek, H., McComas, D., ... others (2010). Energetic neutral atoms from the earth's subsolar magnetopause. *Geophysical Research Letters*, *37*(13).

Galeazzi, M., Gupta, A., Covey, K., & Ursino, E. (2007). Xmm-newton observations of the diffuse x-ray background. *The Astrophysical Journal*, *658*(2), 1081.

Ishikawa, K., Ezoe, Y., Miyoshi, Y., Terada, N., Mitsuda, K., & Ohashi, T. (2013). Suzaku observation of strong solar-wind charge-exchange emission from the terrestrial exosphere during a geomagnetic storm. *Publications of the Astro-*

nomical Society of Japan, *65*(3).

Jansen, F., Lumb, D., Altieri, B., Clavel, J., Ehle, M., Erd, C., ... others (2001). Xmm-newton observatory-i. the spacecraft and operations. *Astronomy & Astrophysics*, *365*(1), L1–L6.

Jensen, J. B., Raeder, J., Maynard, K., & Cramer, W. D. (2017). Particle precipitation effects on convection and the magnetic reconnection rate in earth's magnetosphere. *Journal of Geophysical Research: Space Physics*, *122*(11), 11–413.

Jeřáb, M., Němeček, Z., Šafránková, J., Jelínek, K., & Měrka, J. (2005). Improved bow shock model with dependence on the imf strength. *Planetary and Space Science*, *53*(1-3), 85–93.

Kavosi, S., Spence, H., Fennell, J., Turner, D., Connor, H., & Raeder, J. (2018). Mms/feeps observations of electron microinjections due to kelvin-helmholtz waves and flux transfer events: A case study. *Journal of Geophysical Research: Space Physics*, *123*(7), 5364–5378.

King, J., & Papitashvili, N. (2005). Solar wind spatial scales in and comparisons of hourly wind and ace plasma and magnetic field data. *Journal of Geophysical Research: Space Physics*, *110*(A2).

Kivelson, M. G., & Bagenal, F. (2014). Planetary magnetospheres. In *Encyclopedia of the solar system* (pp. 137–157). Elsevier.

Koutroumpa, D., Lallement, R., Kharchenko, V., Dalgarno, A., Pepino, R., Izmodenov, V., & Quémerais, E. (2006). Charge-transfer induced euv and soft x-ray emissions in the heliosphere. *Astronomy & Astrophysics*, *460*(1), 289–300.

Kuntz, K. (2019). Solar wind charge exchange: an astrophysical nuisance. *The Astronomy and Astrophysics Review*, *27*(1), 1–71.

Kuntz, K., & Snowden, S. (2008). The epic-mos particle-induced background spectra. *Astronomy & Astrophysics*, *478*(2), 575–596.

Kuntz, K. D., Collado-Vega, Y., Collier, M. R., Connor, H., Cravens, T. E., Koutroumpa, D., ... others (2015). The solar wind charge-exchange production factor for hydrogen. *The Astrophysical Journal*, *808*(2), 143.

Lallement, R., Bertaux, J., & Dalaudier, F. (1985). Interplanetary lyman-alpha spectral profiles and intensities for both repulsive and attractive solar force fields predicted absorption pattern by a hydrogen cell. *Astronomy and Astrophysics*, *150*, 21–32.

Lisse, C., Dennerl, K., Englhauser, J., Harden, M., Marshall, F., Mumma, M., ... others (1996). Discovery of x-ray and extreme ultraviolet emission from comet c/hyakutake 1996 b2. *Science*, *274*(5285), 205–209.

Lumb, D., Warwick, R., Page, M., & De Luca, A. (2002). X-ray background measurements with xmm-newton epic. *Astronomy & Astrophysics*, *389*(1), 93–105.

Mitsuda, K., Bautz, M., Inoue, H., Kelley, R. L., Koyama, K., Kunieda, H., ... others (2007). The x-ray observatory suzaku. *Publications of the Astronomical Society of Japan*, *59*(sp1), S1–S7.

Morrison, R., & McCammon, D. (1983). Interstellar photoelectric absorption cross sections, 0.03-10 kev. *The Astrophysical Journal*, *270*, 119–122.

Oliveira, D. M., & Raeder, J. (2015). Impact angle control of interplanetary shock geoeffectiveness: A statistical study. *Journal of Geophysical Research: Space Physics*, *120*(6), 4313–4323.

Østgaard, N., Mende, S., Frey, H., Gladstone, G., & Lauche, H. (2003). Neutral hydrogen density profiles derived from geocoronal imaging. *Journal of Geophysical Research: Space Physics*, *108*(A7).

Pepino, R., Kharchenko, V., Dalgarno, A., & Lallement, R. (2004). Spectra of the x-ray emission induced in the interaction between the solar wind and the heliospheric gas. *The Astrophysical Journal*, *617*(2), 1347.

Raeder, J., Larson, D., Li, W., Kepko, E. L., & Fuller-Rowell, T. (2008). Openggcm simulations for the themis mission. *Space Science Reviews*, *141*(1), 535–555.

Raeder, J., McPherron, R., Frank, L., Kokubun, S., Lu, G., Mukai, T., ... Slavin, J. (2001). Global simulation of the geospace environment modeling substorm challenge event. *Journal of Geophysical Research: Space Physics*, *106*(A1), 381–395.

Robertson, I., Collier, M., Cravens, T., & Fok, M.-C. (2006). X-ray emission from the terrestrial magnetosheath including the cusps. *Journal of Geophysical Research: Space Physics*, *111*(A12).

Shi, Y., Zesta, E., Connor, H., Su, Y.-J., Sutton, E., Huang, C., ... Oliveira, D. (2017). High-latitude thermosphere neutral density response to solar wind dynamic pressure enhancement. *Journal of Geophysical Research: Space Physics*, *122*(11), 11–559.

Shue, J.-H., Song, P., Russell, C., Steinberg, J., Chao, J., Zastenker, G., ... others (1998). Magnetopause location under extreme solar wind conditions. *Journal of Geophysical Research: Space Physics*, *103*(A8), 17691–17700.

Sibeck, D. G., Allen, R., Aryan, H., Bodewits, D., Brandt, P., Branduardi-Raymont, G., ... others (2018). Imaging plasma density structures in the soft x-rays generated by solar wind charge exchange with neutrals. *Space Science Reviews*, *214*(4), 1–124.

Smith, R. K., Brickhouse, N. S., Liedahl, D. A., & Raymond, J. C. (2001). Collisional plasma models with apec/aped: emission-line diagnostics of hydrogen-like and helium-like ions. *The Astrophysical Journal Letters*, *556*(2), L91.

Snowden, S., Egger, R., Freyberg, M., McCammon, D., Plucinsky, P., Sanders, W., ... Voges, W. (1997). Rosat survey diffuse x-ray background maps. ii. *The Astrophysical Journal*, *485*(1), 125.

Strüder, L., Briel, U., Dennerl, K., Hartmann, R., Kendziorra, E., Meidinger, N., ... others (2001). The european photon imaging camera on xmm-newton: the pn-ccd camera. *Astronomy & Astrophysics*, *365*(1), L18–L26.

Turner, M. J., Abbey, A., Arnaud, M., Balasini, M., Barbera, M., Belsole, E., ... others (2001). The european photon imaging camera on xmm-newton: the mos cameras. *Astronomy & Astrophysics*, *365*(1), L27–L35.

Walsh, B., Kuntz, K., Collier, M., Sibeck, D., Snowden, S., & Thomas, N. (2014). Energetic particle impact on x-ray imaging with xmm-newton. *Space Weather*, *12*(6), 387–394.

Weisskopf, M. C., Tananbaum, H. D., Van Speybroeck, L. P., & O'Dell, S. L. (2000). Chandra x-ray observatory (cxo): overview. In *X-ray optics, instruments, and missions iii* (Vol. 4012, pp. 2–16).

Whittaker, I. C., & Sembay, S. (2016). A comparison of empirical and experimental o7+, o8+, and o/h values, with applications to terrestrial solar wind charge exchange. *Geophysical Research Letters*, *43*(14), 7328–7337.

Zoennchen, J., Bailey, J., Nass, U., Gruntman, M., Fahr, H., & Goldstein, J. (2011). The twins exospheric neutral h-density distribution under solar minimum conditions. In *Annales geophysicae* (Vol. 29, pp. 2211–2217).

Zoennchen, J., Nass, U., & Fahr, H. (2013). Exospheric hydrogen density distributions for equinox and summer solstice observed with twins1/2 during solar minimum. In *Annales geophysicae* (Vol. 31, pp. 513–527).

Zoennchen, J., Nass, U., & Fahr, H. (2015). Terrestrial exospheric hydrogen density distributions under solar minimum and solar maximum conditions observed by the twins stereo mission. In *Annales geophysicae* (Vol. 33, pp. 413–426).

Zoennchen, J., Nass, U., Fahr, H. J., & Goldstein, J. (2017). The response of the h geocorona between 3 and 8 r e to geomagnetic disturbances studied using twins stereo lyman-α data. In *Annales geophysicae* (Vol. 35, pp. 171–179).

Figure 1.

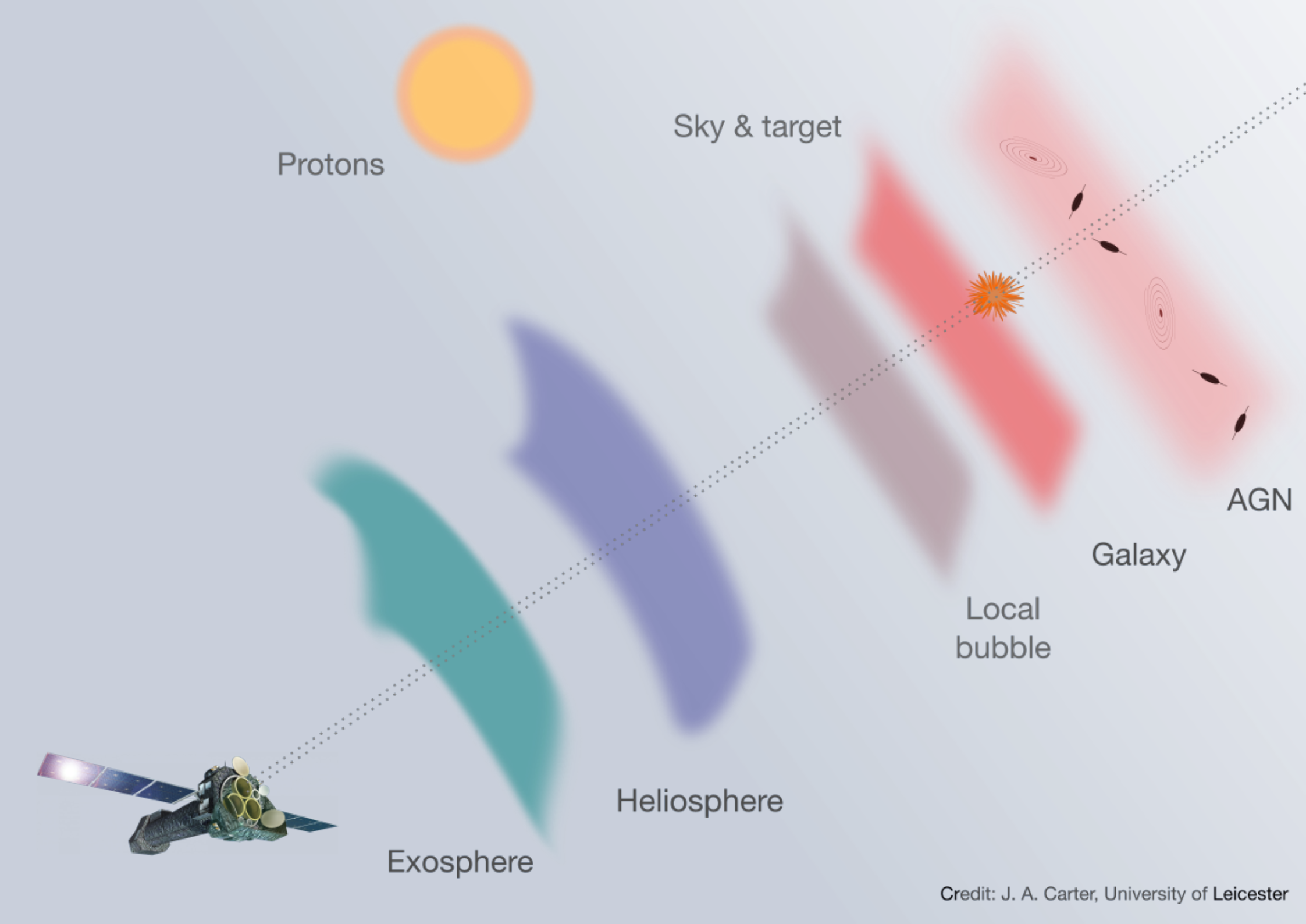

Credit: J. A. Carter, University of Leicester

Figure 2.

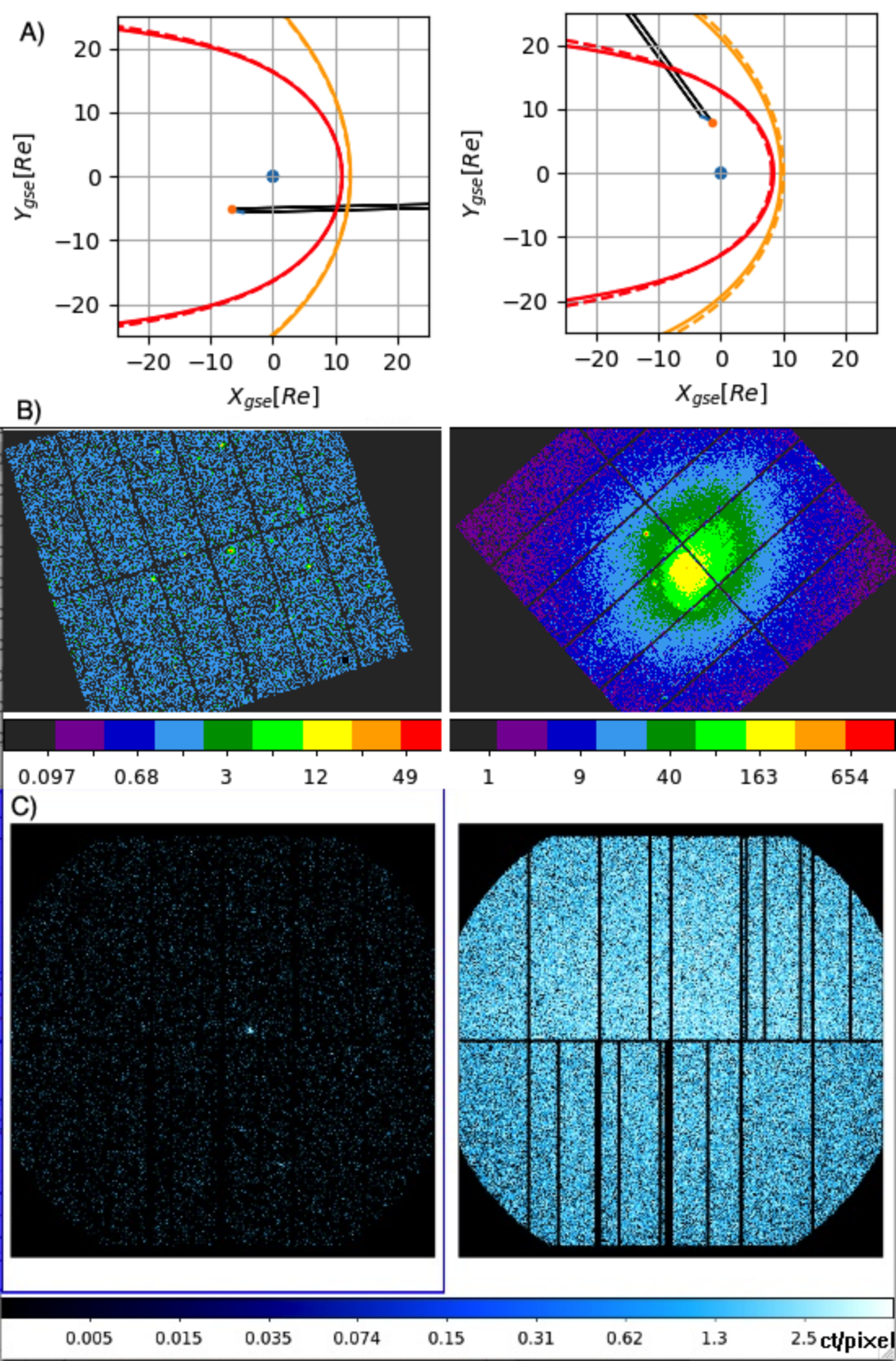
A)
20
10
0
−10
−20
$Y_{gse}[Re]$
−20 −10 0 10 20
$X_{gse}[Re]$
B)
0.097 0.68 3 12 49
1 9 40 163 654
C)
0.005 0.015 0.035 0.074 0.15 0.31 0.62 1.3 2.5 ct/pixel

Figure 3.

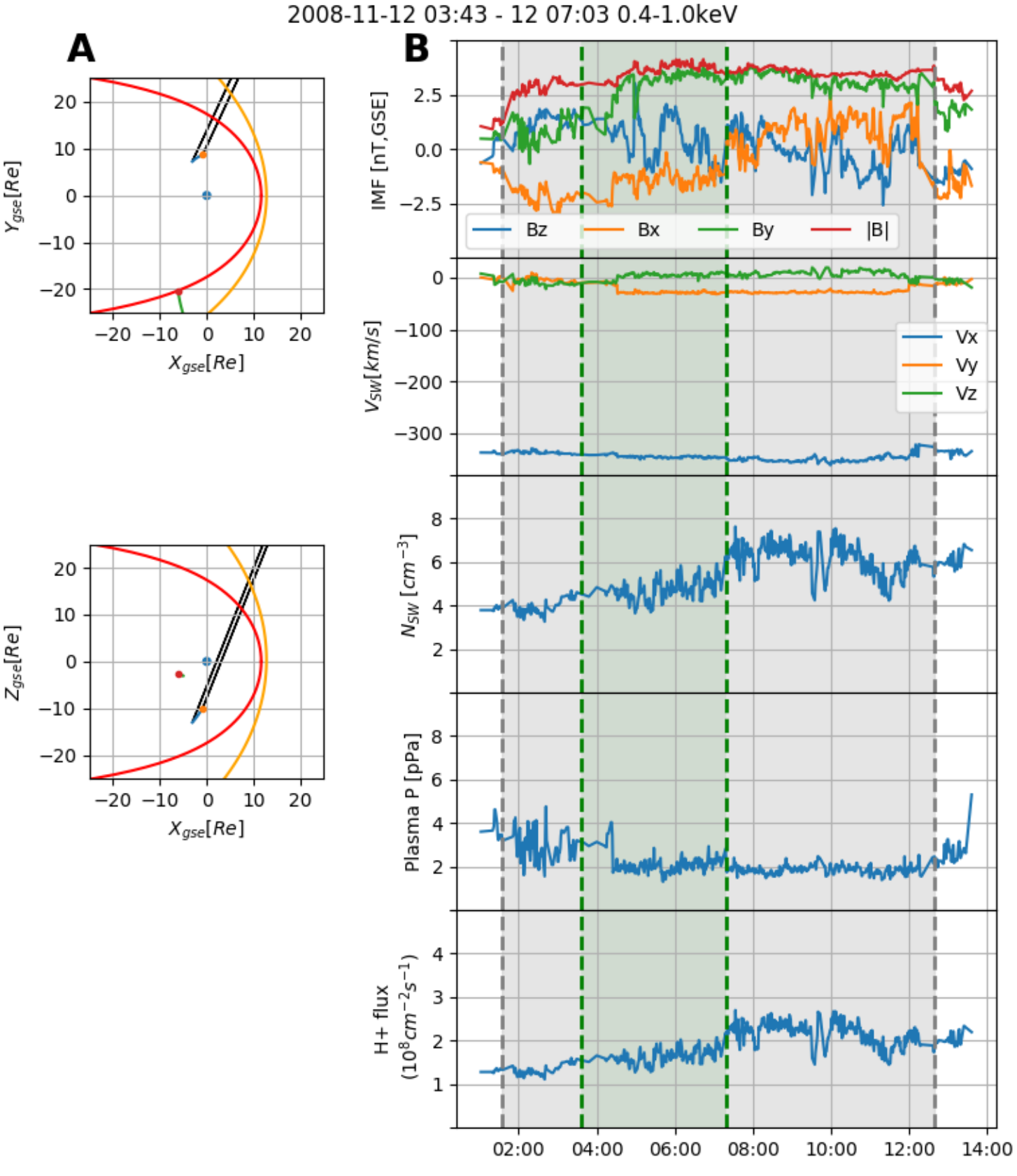
2008-11-12 03:43 - 12 07:03 0.4-1.0keV
A
B
$Y_{gse}[Re]$
$X_{gse}[Re]$
$Z_{gse}[Re]$
$X_{gse}[Re]$
IMF [nT,GSE]
Bz
Bx
By
|B|
$V_{SW}[km/s]$
Vx
Vy
Vz
N_{SW} $[cm^{-3}]$
Plasma P [pPa]
H+ flux
$(10^8 cm^{-2} s^{-1})$
02:00
04:00
06:00
08:00
10:00
12:00
14:00

Figure 4.

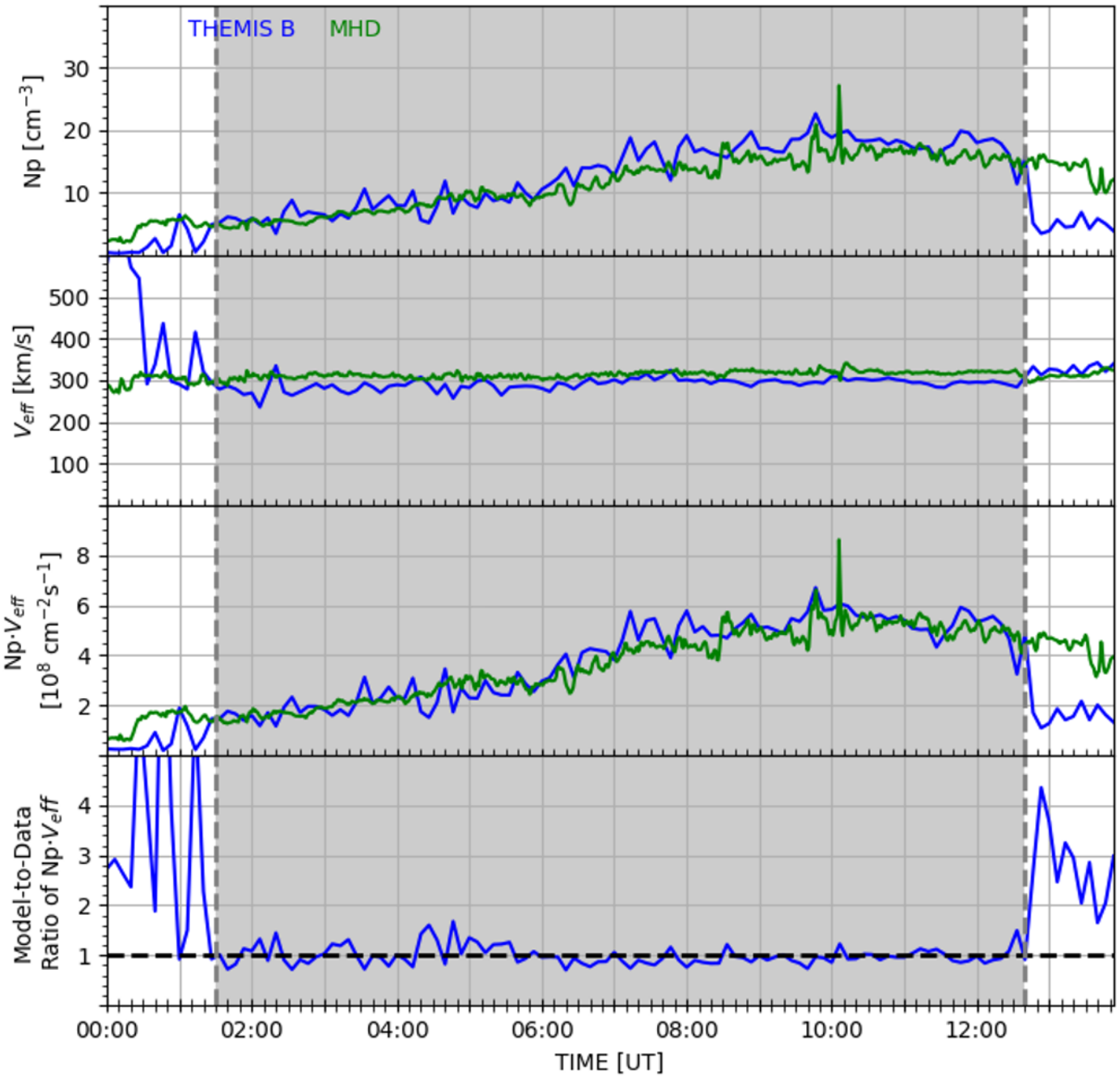
THEMIS B
MHD
Np [cm^{-3}]
V_{eff} [km/s]
Np·V_{eff} [10^8 cm^{-2}s^{-1}]
Model-to-Data Ratio of Np·V_{eff}
00:00
02:00
04:00
06:00
08:00
10:00
12:00
TIME [UT]

Figure 5.

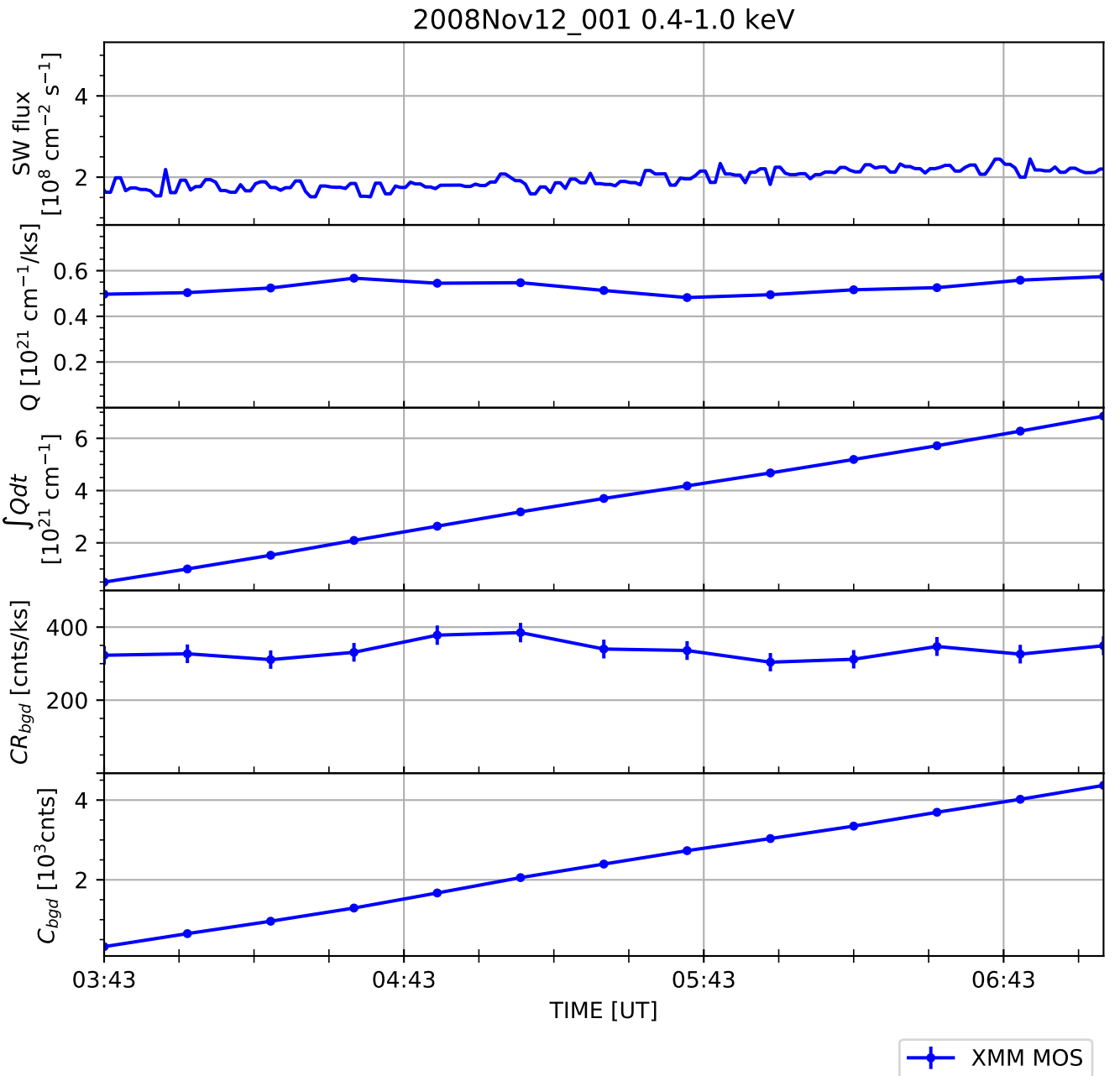

Average neutral density at 10 Re
N_0= 36.8±11.7 cm^{-3}

β = 1.53e-16 cm^4